




OPEN

Gate reflectometry of single-electron box arrays using calibrated low temperature matching networks

Matthew J. Filmer^{1,2}, Matthew Huebner¹, Thomas A. Zirkle^{1,3}, Xavier Jehl⁴, Marc Sanquer^{4,5}, Jonathan D. Chisum¹, Alexei O. Orlov¹ & Gregory L. Snider¹

Sensitive dispersive readouts of single-electron devices (“gate reflectometry”) rely on one-port radio-frequency (RF) reflectometry to read out the state of the sensor. A standard practice in reflectometry measurements is to design an impedance transformer to match the impedance of the load to the characteristic impedance of the transmission line and thus obtain the best sensitivity and signal-to-noise ratio. This is particularly important for measuring large impedances, typical for dispersive readouts of single-electron devices because even a small mismatch will cause a strong signal degradation. When performing RF measurements, a calibration and error correction of the measurement apparatus must be performed in order to remove errors caused by unavoidable non-idealities of the measurement system. Lack of calibration makes optimizing a matching network difficult and ambiguous, and it also prevents a direct quantitative comparison between measurements taken of different devices or on different systems. We propose and demonstrate a simple straightforward method to design and optimize a pi matching network for readouts of devices with large impedance, $Z \geq 1\text{M}\Omega$. It is based on a single low temperature calibrated measurement of an unadjusted network composed of a single L-section followed by a simple calculation to determine a value of the “balancing” capacitor needed to achieve matching conditions for a pi network. We demonstrate that the proposed calibration/error correction technique can be directly applied at low temperature using inexpensive calibration standards. Using proper modeling of the matching networks adjusted for low temperature operation the measurement system can be easily optimized to achieve the best conditions for energy transfer and targeted bandwidth, and can be used for quantitative measurements of the device impedance. In this work we use gate reflectometry to readout the signal generated by arrays of parallel-connected Al-AIOx single-electron boxes. Such arrays can be used as a fast nanoscale voltage sensor for scanning probe applications. We perform measurements of sensitivity and bandwidth for various settings of the matching network connected to arrays and obtain strong agreement with the simulations.

Single-electron devices serving as non-invasive broadband (>1 MHz) sensing elements often employ the one-port radio-frequency (RF) reflectometry to read out the state of the sensor. The so-called gate reflectometry^{1–5} that utilizes existing gates of single-electron transistors (SETs) forming quantum dots (QD) as sensing probes was first used in applications as readout in spin qubit schemes with spin-to-charge conversion^{1,2,6}. There it greatly simplifies the readout circuitry for the whole qubit architecture as it eliminates the need for additional SETs acting as electrometers. The parameter of interest for such “dispersive” readout is the dynamic (or tunneling) capacitance^{7,8} of the QD viewed from the gate $C_{dyn}(V_g)$ that changes in response to a change in QD electron population. The gate-probing approach was also used to study effects of non-adiabatic dissipative processes (the “Sisyphus resistance” effect)⁹ or combinations of both, dispersive and dissipative effects^{10,11} in single-electron devices implemented in metal/metal oxide systems. Recently, gate reflectometry with predominantly dispersive response was used to read out the sensor composed of array of single-electron boxes (SEB) connected in parallel and targeting scanning probe applications^{12,13}. One important constraint for dispersive readout is dictated

¹Department of Electrical Engineering, University of Notre Dame, Notre Dame, IN 46556, USA. ²L3Harris, Fort Wayne, IN 46818, USA. ³Northrop Grumman, Ogden, UT 84405, USA. ⁴Univ. Grenoble Alpes, CEA, Grenoble INP, IRIG, PHELIQS, 38000 Grenoble, France. ⁵Marc Sanquer is deceased. ✉email: mfilmer@alumni.nd.edu

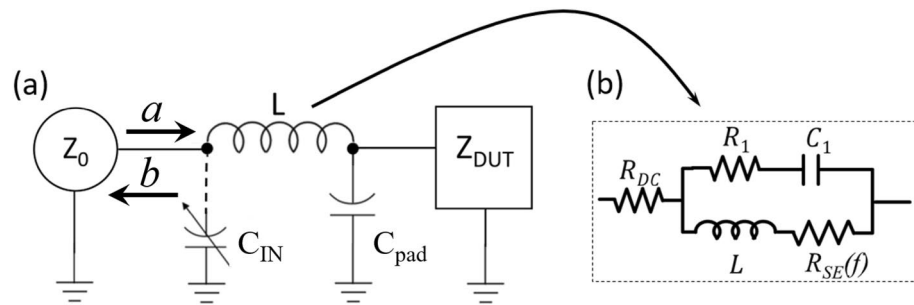


Figure 1. (a) Generic 1-port reflectometry setup. Z_{DUT} is a general representation of a device connected to a MN. This impedance was treated as purely resistive in original RF-SET research¹⁴ where it represents device source-drain resistance $R_{SET}(V_g)$. For gate reflectometry work^{1–5,10,11}, DUT corresponds to predominantly capacitive gate impedance. C_{IN} is a tunable capacitor that enables close matching conditions and is discussed at length in this work. (b) Realistic model of inductors¹⁵ used in experiments^{1–5,10,11}.

by the tunneling rate of electrons at a degeneracy point, $\gamma_0 = k_B T / e^2 R$ where $R \geq 25k \Omega$ is tunnel junction resistance, and T is the temperature. For $f \geq \gamma$ the $C_{dyn}(V_g)$ is greatly reduced and Sisyphus resistance effect dominates¹¹. This limits the range of probing RF frequencies for dispersive readout to ≤ 1 GHz for the majority of Coulomb blockade devices operating at low temperatures (< 4.2 K).

Single port RF reflectometry for nanoelectronic applications was first used to track changes in the source-drain resistance R_{SET} of single-electron transistors¹⁴. Generally speaking, in this case the changes the impedance of the device under test (DUT), Z_{DUT} , are detected using a simple “L-section” matching network (MN) comprising a series off-chip inductor, L , and parallel bonding pad capacitance, C_{pad} , to ground (Fig. 1a) connected to the gate of the DUT. The use of a L-section for the MN enables measurements of DUTs impedances much larger than standard line impedance of 50Ω ($Z_{DUT} = R_{SET} \gg Z_0$) using reflectometry. Near the resonant frequency $f_0 = 1/(2\pi \sqrt{LC_{pad}})$ the MN converts $Z_{DUT} = R_{SET}(V_g = V_{ON}) \approx 100 \text{ k}\Omega$ into impedance of MN with the embedded DUT, Z_{IN}

$$Z_{IN} = L/(C_{pad}R_{SET}) + j\omega L + 1/(j\omega C_{pad}) \quad (1)$$

Here V_{ON} is a gate voltage at which Coulomb blockade is completely or partially lifted, depending on the choice of working point in V_g . By choosing an appropriate value of L , at resonance $Z_{IN} = L/(C_{pad}R_{SET}(V_{ON}))$ can be set to approach Z_0 and thus achieve a significant change in the reflection coefficient $\Delta\Gamma = (Z_{IN} - Z_0)/(Z_{IN} + Z_0) \approx 1$ ¹⁶. The performance optimization for a sensor implies maximization of its signal-to-noise ratio (SNR), which for a drain-coupled RF SET is directly proportional to the change in the magnitude of reflection coefficient as a function of the change in $R_{SET}(V_g)$ ¹⁶.

Similar L-section approach was used for gate-coupled devices studied in^{1–5,10,11}, however, the DUT impedance in Fig. 1a is distinctly different from that of drain-coupled devices^{14,16}. First, this impedance is typically many orders of magnitude larger in value at RF frequencies of interest (100–1000 MHz) ($> 10 \text{ M}\Omega$) and instead of being purely resistive, can in general be represented by a parallel combination of G_{DUT} and C_{DUT} ¹¹, attributed to a combination of Sisyphus resistance⁹ and dynamic capacitance^{7,8}. Clearly, to obtain Z_{IN} approaching Z_0 would require a radical increase in the L/C_{pad} ratio to balance the increase in the Z_{DUT} . In practice, $C_{pad} \geq 0.1 \text{ pF}$, so for large $Z_{DUT} \gg 1 \text{ M}\Omega$ the $Z_{IN} \ll Z_0$ and the DUT is always overcoupled to the feedline¹⁶. As a result it is impossible to reach close to match conditions with the simple L-section MN. However, if the off-chip inductor is judiciously selected, an additional parallel capacitor (C_{IN} in Fig. 1a) forms a Π MN¹⁷ that can be designed to achieve good match for the case when $Z_{IN} \ll Z_0$ for $C_{IN}=0$. The simplicity of this approach with an off-chip inductor L , a given pad capacitor C_{pad} and balancing capacitor C_{IN} makes it an attractive option for the design of the MN. The most common inductors used in these applications are ceramic core surface mount inductors in the range 100–1000 nH (for example, 0805CS Coilcraft Ceramic Chip Inductors¹⁵) which enables the operation in the range 0.1–1 GHz. These inductors have small dimensions which allows their placement in very close proximity to the nanodevice under test. It is, however, very important to take into account the non-idealities of components used in the design of the Π MN, with the inductor being the dominant source of non-ideality.

Recently, Ares et al.¹⁸ attempted to design and use a Π MN using a 5 element circuit model (Fig. 1b). However, the parameters of the circuit model used by Ares¹⁸ are only known at $T = 293 \text{ K}$, while direct characterization of inductors reveals a very significant change in the DC resistance of the inductor with lowering temperature (by a factor ~ 70 for $T \leq 10 \text{ K}$ ¹³) and there are likely changes in the parameters of other parasitic elements, so that no accurate quantitative comparison is possible between the 300 K model and experimental results at $T \leq 10 \text{ K}$. Since the value of C_{IN} in this case cannot be accurately calculated to obtain close match, Ares et al.¹⁸ utilized a varactor as a variable capacitor C_{IN} to empirically reach a matching condition. They demonstrated that by obtaining a close match the sensitivity of the circuit to the variations in device capacitance can be improved. Their results also indicate that below 1 K the GaAs varactor has diminished range of operation due to carrier freeze out. To avoid this problem, a fixed-value capacitor can be used instead. However, this requires a good understanding of the low temperature behavior of the MN components. Indeed, even if a good match could be accurately predicted at room temperature using manufacturer’s models, the parasitics of the inductors exhibit a

strong temperature dependence, thus changing the parameters of the network which in turn results in a different value of C_{IN} required to achieve match. The importance of properly accounting for parasitic elements of the circuit and their temperature dependence was clearly demonstrated in recent publications^{13,19}.

As we show below, proper account for parasitic parameters also has very significant impact on the accessible bandwidth (see part S3, S4, and S7 in Supplementary materials for more details). This shows the paramount importance of proper model considerations in avoiding gross errors in the design of matching network and, consequently, interpreting the results of experiments. In this context, one important issue which is often overlooked in the experimental literature is the need for a properly calibrated experimental RF setup. Reflectometry measurements can only be quantitatively correct if the measurement system is calibrated against known standards. This means, for example, that at a calibrated reference plane, both open and short standards are expected to produce $|\Gamma| = 1$ and a matched load should produce $|\Gamma| = 0$. Experimental setups never produce these results without the use of error correction because of a wide range of non-idealities in the signal paths (standing wave resonances in the transmission lines, deviations from exact Z_0 , matched values in components used, frequency dependent transfer characteristics and phase shifts in the amplifiers and couplers, etc.). To be able to accurately correlate RF measurements to models, it is therefore critical to error correct the measured data through calibration, a standard practice when measuring S-parameters with a network analyzer. The Calibration and Error Correction (CEC) is a standard practice for room temperature RF measurements, and room-temperature RF instrumentation²⁰ but it is not typically performed for low temperature reflectometry, and uncalibrated data are, with a few exceptions²¹, reported in the literature. Here we demonstrate that the standard Short-Open-Load CEC protocol can be directly applied at low temperature using inexpensive calibration standards and thus a) greatly simplify the design of MN and b) obtain the data that can be quantitatively compared with the DUT models. Strictly speaking, without proper calibration only qualitative analysis is possible.

The goal of this work is to develop a simple method to construct high quality, resonant MNs for measuring large impedances $\geq 10\text{M}\Omega$ typical for gate-sensing reflectometry and accurately evaluate its sensitivity and the available measurement bandwidth using a well-characterized DUT.

In this work we utilize arrays of Al-AlO_x single-electron boxes²² (SEBA) connected in parallel^{12,13} shown in Fig. 3a–c fabricated on fused silica substrates. The impedance of SEB can be adequately modeled as a parallel combination of R_{DUT} and C_{DUT} using a model proposed in¹¹. The target application of this device is a voltage sensitive high-speed scanning probe^{12,13,23,24}. The use of parallel-connected single-electron devices sharing common gate results in incoherent oscillation pattern²⁵ in the amplitude of Coulomb blockade oscillations that scales up as $N^{1/2}$. In case of SEBA the use of arrays with $N \geq 100$ makes the magnitude of composite response comparable to that of an RF-SET^{12,13}.

Importantly, the Al – AlO_x single-electron boxes^{9,12,13} fabricated by Dolan-bridge technique²⁶ have much higher tolerance to electrostatic discharge events compared to other (e.g. fabricated by CMOS^{1–3}) single-electron devices. Since there is no DC current path through SEB, there is no DC voltage across the junction. However, if a step voltage, V_g , is abruptly applied to an SEB, it will be divided between C_g and C_j until C_j discharges through R_j so that the voltage across the junction can instantaneously reach $V_j \approx C_j / (C_j + C_g) \times V_g$. Here C_g is gate capacitance and C_j and R_j are junction capacitance and resistance. The gate capacitor of SEB C_g is formed by the metal line separated (horizontal line in the middle of Fig. 3d) from SET island by a thick ($t \geq 100$ nm) dielectric with a high breakdown voltage while the junction (C_j , R_j) is formed by the source wire overlapping the metal island with tunnel-transparent dielectric ($t \approx 1$ nm) in between. For the devices studied in this work $C_j / C_g \geq 10$, so that if a voltage is abruptly applied across SEB, the voltage across the junction is attenuated by a factor of ≥ 10 . The experimental evidence confirms that arrays of single-electron boxes studied in this work provide a robust DUT for our study which can be subjected to multiple cooling/heating cycles and can withstand soldering/desoldering of electronic components attached to “live” devices.

Experimental method

Experimental setup. A simplified schematic diagram of the experimental setup used in this work is presented in Fig. 2a. Low temperature data are obtained in a closed cycle refrigerator with a base temperature of 3.6 K (by Advanced Research Systems). Signal generation and data acquisition are performed using a digital Zurich Instruments UHF Lock-In Amplifier (UHF LIA) capable of full homodyne and modulation detection of signals up to 600 MHz²⁷. The UHF LIA produces the forward wave of the reflectometer \tilde{a} at f_{RF} which goes through a -20dB attenuator at room temperature, another -20 dB attenuator by CRYSTEK and a directional coupler (ZFDC-20-50+) thermally anchored at the second stage at 3.6K to produce the incident wave a at the reference plane (RP) of the MN and DUT. The reflected wave b returns through the system to the UHF LIA (b). To combat the accumulated losses and improve the SNR we use low noise amplifiers by Minicircuits: the first stage, ZX60-P33ULN+, (A1 in Fig. 2a) located at the 1st stage of the cryocooler at $T \approx 40$ K, and two stages, ZX60-P103LN+, at room temperature (A2 in Fig. 2a), for a total gain ≈ 70 dB at 500 MHz. Special care is taken to avoid the variation of gain over time in both cold and warm amplifiers, for which regulated power supplies with stable output voltage (+ 5 V for warm amplifiers and + 2.7 V for cold amplifiers) are used throughout the experiment.

The system calibration and error correction is performed as described below in “[Calibration and error correction](#)”. As a result of CEC, the errors between reference plane and input of the UHF LIA are eliminated. This enables experimental determination of MN settings that achieves a match using a technique described in details in “[Optimization of matching network](#)” employing a minimal knowledge of parasitic parameters of the inductor L and C_{pad} used in Π MN for a variety of high impedance DUTs, $Z_{DUT} \geq 10\text{M}\Omega$.

For the experiments described in “[Gate reflectometry: sensitivity and bandwidth tuning](#)” we utilize the UHF-MOD AM/FM Modulation option in digital ZI UHF²⁷ which allows simultaneous extraction of sidebands (SB)

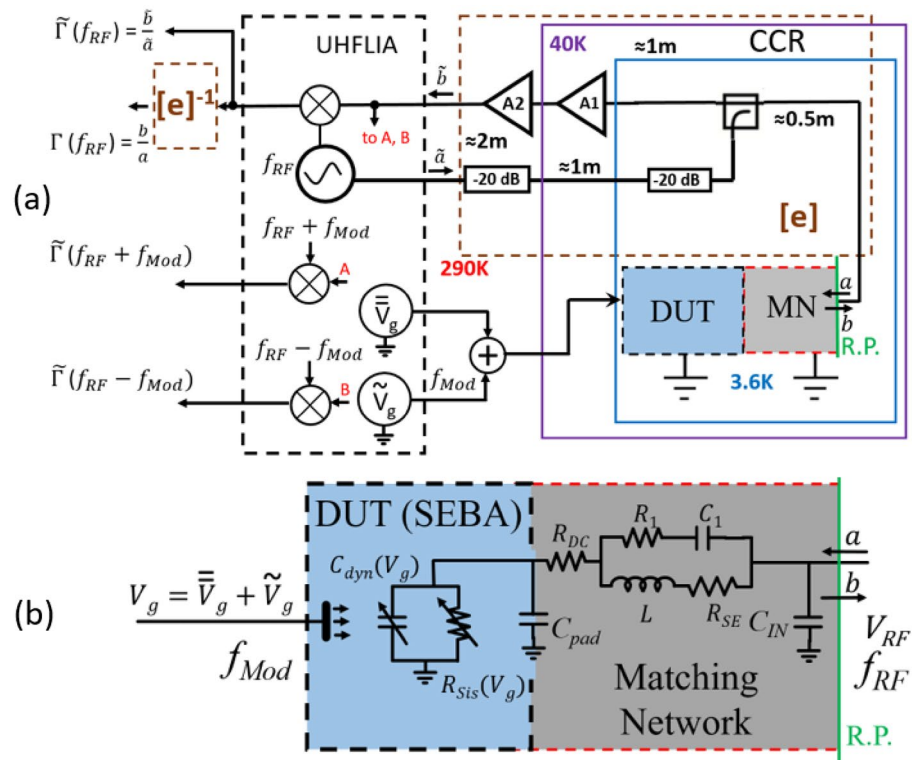


Figure 2. (a) Experimental setup. Components surrounded by a violet line are inside close cycle refrigerator (CCR), with cold amplifier A1 at 40 K. Components within blue box are at $T = 3.6$ K. Dashed brown box labeled “[e]⁻¹” contains all the components that contribute to non-idealities (“errors”) in the reflectometry process. Dashed brown box labeled “[e]” is an “error-correction box” implemented in software that generates error corrected data (ECD) by using calibrated standards to calculate error correction coefficients. UHFLIA is ZI UHF lock-in amplifier which generates all signals and performs demodulation. Dashed green line delineates the reference plane (R.P.). (b) Zoom-in into a combination of DUT and MN showing all of the circuit components. DUT is represented by SEBA; the SEBA admittance is controlled by the gate voltage V_g . Pad capacitance, C_{pad} , is shown as an element shared between MN and DUT.

for the amplitude modulated signal applied to the gates of SEBA by performing synchronous demodulation at three frequencies: $f_{RF} - f_{Mod}$, f_{RF} , and $f_{RF} + f_{Mod}$. For that purpose a small modulating signal \tilde{V}_g superimposed with DC gate bias \bar{V}_g is applied to the gates of SEBA. In this work we do not apply CEC protocol for the SB signals. The ZI UHF lock-in allows implementation of error correction on SB before the demodulators, this option will be explored in our future work.

Calibration and error correction. In this work, we follow a one port *Short-Open-Load* (SOL) calibration/error correction protocol. To do so a collection of three known terminations are prepared and measured on a printed circuit board identical to the actual board containing MN elements and DUT (i.e., the calibration board is identical by design to the one used in the experiment, fabricated in the same batch from a single drawing file) and error correction coefficients are computed for chosen temperatures (in the context of this paper, 300 K and 3.6 K). The detailed description of error correction protocol, SOL calibration kit and its use are presented in part S1 of the Supplementary materials. All circuit elements are inside the brown dashed box, labeled “e” in Fig. 2a (i.e. cables, amplifiers, directional coupler, attenuators) introduce unavoidable errors due to their frequency dependent characteristics. By performing calibration we create an “error-correction box”, labeled “[e]⁻¹” in Fig. 2a so that the acquired raw data can be error-corrected to yield an “error-free” $\Gamma(f_{RF})$ signal. By using error correction we in effect move the reference plane from the input of UHF LIA to the output of the reflecting element, i.e. to the MN with the attached DUT (Fig. 2b). The green dashed line in Fig. 2a indicates the position of the reference plane after CEC; in practice this corresponds to the solder joint of the inductor L and balancing capacitor C_{IN} (see Fig. S3 in Supplementary materials). An example of experimental data before and after error correction is presented in Fig. S4 in Supplementary materials.

Optimization of matching network. The design of any circuit begins with a reliable model of the actual components being used. A minimal knowledge of the pad capacitance enables crude evaluation of the desired operating frequency based upon available inductor values: $f = 1/2\pi\sqrt{LC}$ (the actual resonance frequency can be up to 20% lower due to parasitic parallel components, Fig. 1b).

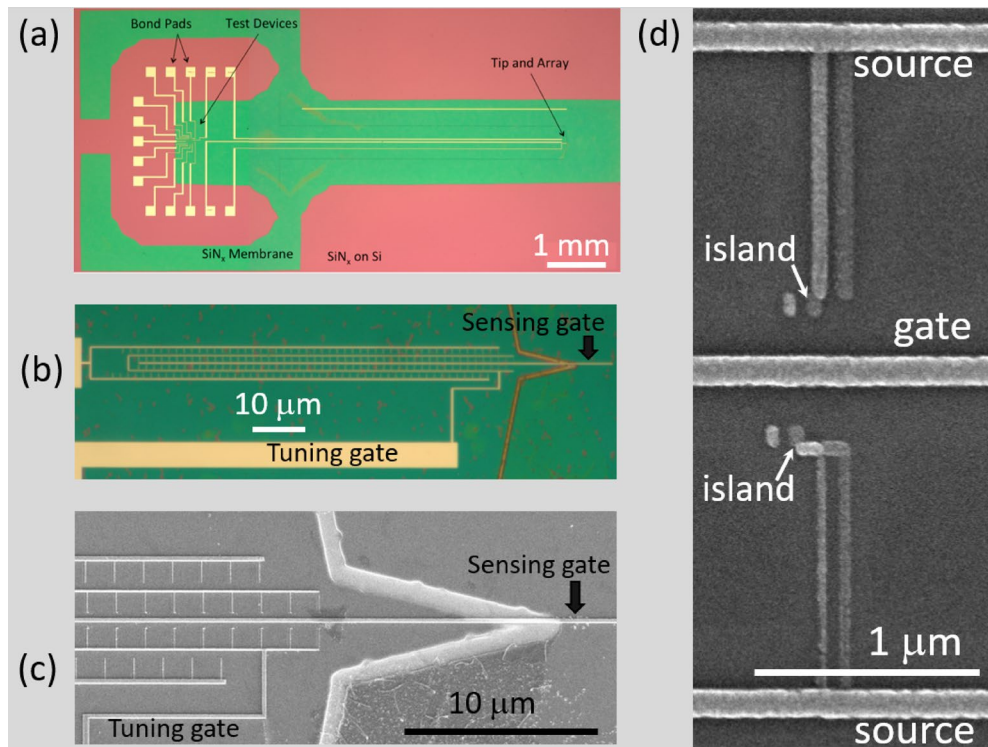


Figure 3. Micrographs of $Al - AlO_x$ SEBA fabricated using Dolan bridge technique (a) Optical micrograph of the SEBA on SiN_x membrane (green) fabricated on top of oxidized Si wafer. (b) Zoom-in view showing SEBA with 2 gates (sensing and tuning). The trench defining the tip is etched into Si membrane using reactive ion etching (c) Electron micrograph of SEBA (30 SEBs are visible out of 200 total) on SiN_x substrate. (d) Electron micrograph of two SEBs, the sensing gate is in the middle. All of the devices studied in this work are fabricated on fused silica substrate.

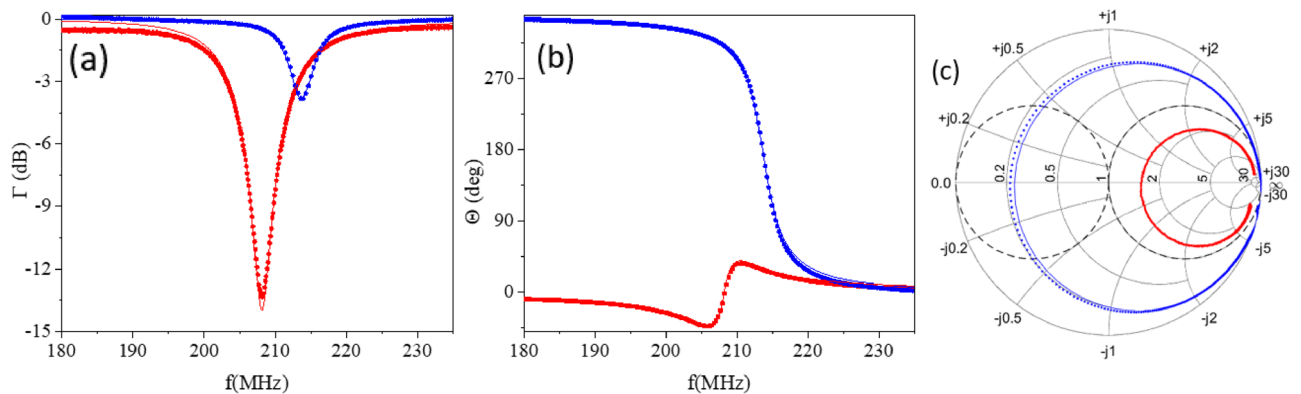


Figure 4. Results of reflectometry measurements at $T=300K$ and $3.6K$ for MN composed of $L=820$ nH inductor and C_{pad} with no DUT present; error-corrected data are shown: (a) magnitude measurements; (b) phase measurements; (c) Smith chart. Dots—experiment, solid lines—calculations. Red: 300 K, blue: 3.6 K. Simulations are performed based on 820 nH inductor Coilcraft model¹⁵ adjusted for low temperature.

In our experiments, the value of C_{pad} is on the order of 0.5 pF. Here we accumulated all capacitances to ground in parallel with the DUT (e.g. bond wire to ground) into C_{pad} .

To construct the MN we use off the shelf inductors by Coilcraft¹⁵ with unknown parasitics at low temperature. The selected inductor is installed on the board, thus creating a DUT + MN combination attached at a reference plane as shown Fig. 2b. The frequency response of the partially assembled MN is acquired at the intended operation temperature for which calibration is performed and error-correction is applied. To illustrate the change in the tuning of MN caused by temperature the experiment that involves only L and C_{pad} , i.e. with no Z_{DUT} connected, is performed. Note that the capacitance of the DUT studied in this work is at least 10^3 smaller than C_{pad} so the change in the reflected signal with DUT added would be below the resolution limit in Fig. 4. The results of the

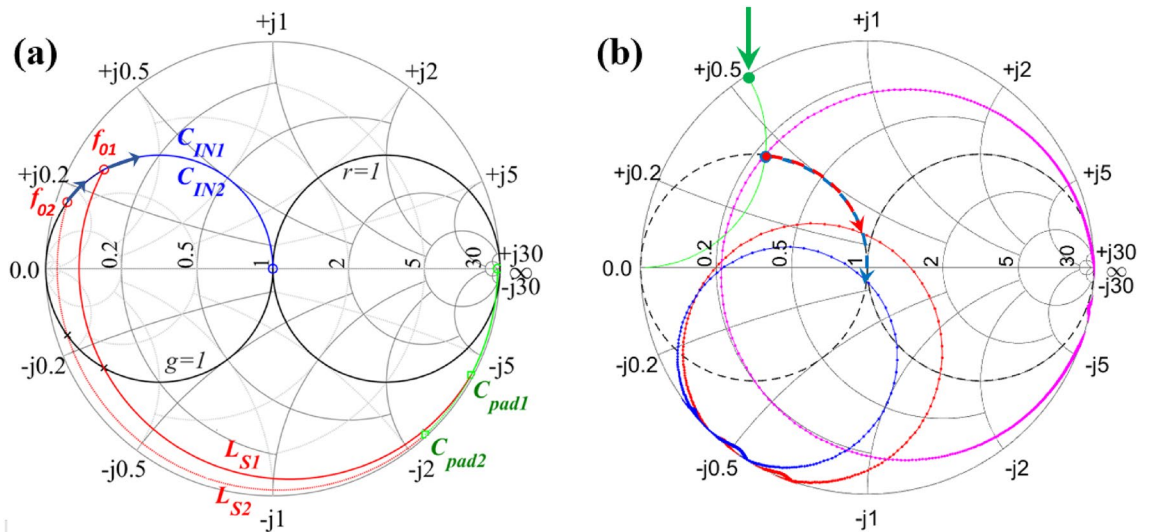


Figure 5. (a) The impedance trajectory sketch showing how to obtain the matched load. Green arcs represent the resulting effect of pad capacitance C_{pad} added in parallel with DUT. Two cases are shown for two different values of pad capacitance, with a shorter green arc corresponding to a smaller C_{pad} . (b) Experimental results obtained using ECD. Magenta arc represent the result of reflectometry measurement shown in Fig. 4 for 3.6 K. Green line towards the periphery follows the constant susceptance curve and reaches the edge of the Smith chart at the point indicated by a green dot and green arrow. This value of susceptance is used in calculation of required $C_{IN} = 24$ pF which moves the impedance to the center of the Smith chart (blue arrows). Blue arc—experimental data for $C_{IN} = 27$ pF; red arc— $C_{IN} = 20$ pF.

experiment for $L = 820$ nH and C_{pad} are presented in Fig. 4 where magnitude and phase plotted vs frequency (Fig. 4a,b) and in the Smith chart (Fig. 4c) for two temperatures, 300 K (in red), and 3.6 K (in blue).

The data acquired at room temperature (red dots in Fig. 4) are in very good correlation with the Coilcraft model¹⁵ for the $L = 820$ nH inductor and $C_{pad} = 458$ fF, with C_{pad} being the only adjustable parameter which sets the operating frequency. However, the data acquired at low temperature 3.6 K (blue dots in Fig. 4) clearly indicate that parameters of the MN change significantly with temperature. This presents a challenge when trying to design a MN using components for which good models are only available at room temperature. Fortunately, precise model parameters are not needed if the impedance can be measured directly using an error-corrected system. To better understand the change in parasitic components of the inductor caused by the reduction of temperature we performed simulations of the frequency response of MN composed of LC_{pad} section and compared it with the experiment (see Supplementary materials, Sect. S5 for details). In simulations we took into account experimentally observed reduction of the series coil resistance due to reduction of resistivity and associated reduction of skin-effect resistance¹³. The results of the simulations indicate that the components associated with core loss (R_1 , C_1 in Fig. 1b) also change with temperature. These changes in the MN parameters result in the expansion of the impedance trajectory vs frequency in the Smith chart out of $r = 1$ circle with lowering of the temperature. This change in the impedance trajectory is crucially important for the success of the proposed method limiting it to the designs of MNs for which $Z_{IN} < Z_0$, i.e. when Z_{IN} without balancing capacitor (i.e. for $C_{IN} = 0$) is overcoupled to the feedline at operation temperature; otherwise different MN solutions may be applied but they are beyond the scope of this paper.

Figure 5a illustrates the procedure we utilize to determine the value of the component C_{IN} in the MN. We will start our analysis with the (unrealistic) case when $C_{pad} = 0$ and then add components to modify Z_{IN} . Initially, since $Z_{DUT} \gg Z_0$, the impedance trajectory vs carrier frequency is situated very close to the right border of the Smith chart, within the $r = 1$ circle in Fig. 5 making it very far away from the matching point. However, parasitic pad capacitance C_{pad} moves the impedance trajectory outside the $r = 1$ circle, green arcs in Fig. 5a. Two green arcs are shown in Fig. 5a with a longer arc corresponding to a larger C_{pad} , which in practice may correspond to the same size pad but on a different substrate (for example, switching from SiO_2 to SiN_x for C_{pad} results in the increase of dielectric constant by a factor of $9.5/3.9 \approx 2.4$ thus increasing the C_{pad} by the same amount). Alternatively, the same analysis can be applied for the same C_{pad} at two different target frequencies, with longer arc corresponding to the higher frequency. To reach matching condition an impedance transformer is required to raise the real-part of the impedance. A series inductor L_{S1} moves the impedance trajectory clockwise along a constant resistance circle. The addition of the inductor needs to move the impedance trajectory inside the Smith chart so that it intersects the matched admittance circle $g = 1$ at some frequency f_{01} in the upper half of the Smith chart, corresponding to a capacitance in parallel with $L_{S1}C_{pad}$ section. That frequency, f_{01} , becomes the operating frequency of the matching network, f_{Op} . Depending on the application, for a different C_{pad} the user may either choose a different inductor (e.g., a $L_{S2} < L_{S1}$ for a larger C_{pad} in Fig. 5a) so that the operating frequency stays approximately the same $f_{01} \approx f_{02}$, or keep the same inductor L_{S1} and allow operating frequency to change. It is important to note that in case of $Z_{DUT} \gg 1M$ this is possible only if added inductor has some parasitic

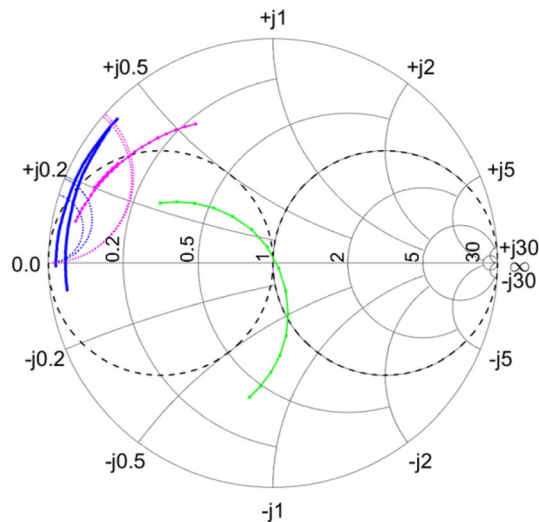


Figure 6. Smith chart showing impedance trajectories for ECD reflectometry measurements using two similar calibrations for MN composed of $L = 240$ nH inductor and $C_{IN} = 0$ (blue dots), 15 pF (magenta dots), 30 pF (green dots). Imperfections in calibration results in uncertain definition of C_{IN} needed to achieve good match for $C_{IN} = 0$. A "half-capacitance" guess (magenta dots) results in a much more accurate determination of C_{IN} .

dissipative component on the order of Z_0 in form of coil resistance or loss in the core, which is exactly the case for the inductors used in this work. Otherwise, the expanded impedance trajectory runs too close to the edge of the Smith chart and as we show below determination of C_{pad} using the proposed method becomes problematic.

Once the crossing of the $g = 1$ circle is ensured, a balancing capacitor C_{IN} in parallel with LC_{pad} is introduced to eliminate the remaining reactance and thus move the impedance trajectory to the center of the Smith chart at f_{Op} . To compute the required C_{IN} , the susceptance b of MN at f_{Op} must be equal to the susceptance of a capacitor C_{IN} that is needed to reach a match point.

$$\frac{jb}{Z_0} = j2\pi f C_{IN}, \quad (2)$$

so that

$$C_{IN} = \frac{b}{2\pi f Z_0}. \quad (3)$$

Using this technique, an optimal value of C_{IN} is calculated according to Eq. (3). This capacitor must be installed on the board next to the inductor's input terminal to keep its close proximity to the calibration reference plane. Clearly, the added capacitor C_{IN} must keep the same value and low loss within the entire temperature range. We use high Q/low ESR ceramic capacitors by Johanson Technology for which the experimentally observed variation of $C_{IN} < 2\%$ from 300 K to 3.6 K¹³ ensures the validity of this approach. The use of balancing capacitor C_{IN} for reaching the matching conditions limits the range of impedances that can be matched with this method, yet the highly resistive types of DUTs discussed here fall within the range of acceptable impedances.

Let us consider the case $L = 820$ nH for which the impedance trajectory lies within $r = 1$ circle at room temperature, red arc in Fig. 4c. Importantly, at low temperature 3.6K the impedance trajectory expands out of it and crossing $g = 1$ in the upper part the Smith chart thus making it possible to find an appropriate positive value of C_{IN} . The addition of balancing capacitor C_{IN} translates operating point very close to the middle of the Smith chart, i.e. to the match point. From the data shown in Fig. 5b we calculated $C_{IN} \approx 26$ pF. Optimization of C_{IN} value performed in ADS software yields very similar result. To confirm the validity of our considerations we performed measurements using two close values of C_{IN} , 20 and 27 pF. The results are presented in Fig. 5b as two trajectories: red, which corresponds to $C_{IN} = 20$ pF and blue, which corresponds to $C_{IN} = 27$ pF. As expected, both capacitors result in a close match, with $C_{IN} = 20$ pF case corresponding to a slightly overcoupled MN, and $C_{IN} = 27$ pF to a slightly undercoupled MN. We need to point out that determination of balancing capacitor may represent a challenge if MN impedance trajectory for C_{IN} expands very close to the edge of the Smith chart thus reducing the accuracy of C_{IN} determination.

Let us now proceed with the case where $L = 240$ nH is connected in series with $C_{pad} = 467$ fF (see Sect. S5 in the Supplementary materials on how it is extracted) and DUT connected in parallel to C_{pad} ; note that all the experimental data except Fig. 4 are acquired with that DUT. The two blue traces in Fig. 6 that cross the $g = 1$ circle there are experimentally obtained at very close temperatures 3.6K and 4K. However, calibration inaccuracy for heavily overcoupled MNs, when the impact of error correction on impedance trajectory is very significant, results in distinctly different impedance trajectories and two different constant susceptance curves (two blue dashed lines in Fig. 6) that determine C_{IN} . In addition to that, the low resolution of the Smith chart for impedance

$Z_{IN} \approx 0$ makes it harder to determine the correct C_{IN} . The values obtained from the chart using Eq. (3) are in the range 39 to 45 pF. Therefore, for more accurate determination of C_{IN} a smaller (e.g. 2 times smaller) than needed for match capacitor can be used to do a "pre-match" experiment, so that the method from "Optimization of matching network" can still be applied but with far more accurate result. Indeed, in this case for $L = 240$ nH by adding a small "pre-match" capacitor $C_{IN}=15$ pF, the impedance trajectory changes (magenta dots, the results again obtained using two calibrations, 3.6K and 4K in Fig. 6), due to much better defined resonance. The impact of imperfect error correction is less significant, and both traces are overlapped. The crossing of the $g = 1$ circle then results in two overlapping constant susceptance traces that cross the Smith chart edge with the suggested value of an extra 20 pF needed in addition to the existing 15 pF, thus making the suggested $C_{IN} = 15 + 20 \approx 35$ pF.

Gate reflectometry: sensitivity and bandwidth tuning. The intent of the method explained above in "Optimization of matching network" is to achieve close to matching conditions in order to yield the best SNR. However, in experiment the optimal conditions for sensing may represent a trade off between the largest SNR and the bandwidth (BW) available to perform sensing using a DUT. Here we experimentally investigate various settings for MN to determine the optimal operating conditions and adjust it depending on the task of the sensing. For this experiment we use MN characterized in Fig. 6 ($L = 240$ nH, $C_{pad} = 467$ fF) and utilized a SEBA composed of 200 nominally identical single-electron boxes as the DUT to conduct these measurements^{12,13}

To map out the influence of the balancing capacitor C_{IN} on SNR and BW we perform six cycles of low-temperature measurements for C_{IN} set at 0, 6.8 pF, 15 pF, 30 pF, 46.8 pF and 60 pF. For each experiment the selected C_{IN} is soldered to the central line of the co-planar waveguide (CPW), like it is shown in Fig. S3 in the Supplementary materials, while keeping connection to the SEBA intact.

In each measurement cycle we first characterize the MN by sweeping the carrier frequency f_{RF} and determine the optimal RF frequency f_{Op} for a given C_{IN} using error-corrected data to find a minimum of $|\Gamma|$. In this process we also model MN using parasitics of the inductor adjusted for low temperature and found very good agreement between the error-corrected data and simulations (see Sect. S5 in Supplementary materials for details). From the Smith charts in Fig. 6 it is clear that the closest to match point conditions are observed for $C_{IN} = 30$ pF, while for larger C_{IN} the DUT impedance Z_{IN} is undercoupled ($Z_{IN} > Z_0$) and for smaller C_{IN} it is overcoupled ($Z_{IN} < Z_0$) to the feedline.

Once operating frequency is determined in each measurement cycle for each C_{IN} by finding a minimum in an error-corrected value of $|\Gamma|$, we measure the magnitude of the demodulated signal as a function of gate voltage V_g (no modulating signal is applied to the gate for this experiment). The oscillations of magnitude (a) and phase (b) of reflection coefficient in response to the variation of gate voltage applied to SEBA are plotted in Fig. 7 for three different values of C_{IN} in the MN. These oscillations represent a beating pattern resulting from asynchronous single-electron charging of the SEBs in the array^{12,13}. Since random offset charges are changing with every thermal cycle no close correlation in oscillations shape between thermal cycles is expected¹³.

The data shown in Fig. 7a,b are error corrected and therefore can be directly compared quantitatively. Note that the distribution of phase and magnitude components in the "raw" (Fig. S9 in Supplementary materials) signal differs drastically from error-corrected data. Figure S9 shows that the raw data show very weak oscillations in magnitude of reflection $\Delta\Gamma(V_g)$, and strong oscillations in phase $\Delta\Theta(V_g)$, in a stark contrast with error-corrected data where oscillations are visible in both components. This example shows that without proper calibration the interpretation of the results based on raw data (e.g. a statement claiming that measured phase shift is solely due to a capacitive change in the Z_{DUT}) can be misleading.

As expected, the signal strength is greatly enhanced when a well-matched MN is used. It is important to note that for both cases away from matching the demodulated signal contains > 10 times larger DC component (i.e. DC offset independent on V_g that must be subtracted in order to plot it in one figure, see Fig. S7 in Supplementary materials). This corresponds to the reduction of modulation depth produced by the Coulomb blockade oscillations in the SEBA in case of poor matching.

For more accurate quantitative evaluation of SNR and available bandwidth and their dependence on C_{IN} we utilize the setup Fig. 2b with gate modulation signal, \tilde{V}_g , turned on. In this case a small sinusoidal signal \tilde{V}_g at a frequency $f_{Mod} \ll f_{Op}$ is applied to the gate of the SEBA. The sweep of gate voltage V_g modulates the admittance of SEBA^{12,13} which results in generation of sidebands (SBs) in the reflected signal $f_{Op} \pm f_{Mod}$ ¹⁴. Analysis of SB signals enables significantly more accurate evaluation of SNR and BW because it eliminates the DC background along with $1/f$ noise present in the demodulated carrier signal and instead performs synchronous detection of the signal in the narrow band (≈ 1 Hz) near $f_{Op} \pm f_{Mod}$ defined by the demodulator time constant (30 ms).

An example of experimentally obtained SEBA oscillations in the SB magnitude acquired over $\pm 0.9 V_g$ range (curves are horizontally offset for clarity) for six different values of C_{IN} is presented in Fig. 7c.

The RMS amplitude of the modulating signal at $f_{Mod} = 8$ kHz is 3.5 mV, corresponding to an oscillating charge of $\approx 0.07e$ applied to the gate of SEBA. The amplitude of modulating signal is chosen to operate within a linear part of the slope $d|\Gamma|/dV_g$ of the oscillation in Fig. 7a,b the by sweeping the magnitude of \tilde{V}_g and making sure the magnitude of SB signal scales linearly with increase in \tilde{V}_g . Likewise, the amplitude of the carrier signal is selected to operate in the linear regime. This is achieved by sweeping the RF carrier amplitude and ensuring the magnitude of SBs scales linearly with increasing RF amplitude. The peak RF amplitude (\tilde{a} in Fig. 2a) is then fixed at a level of 100 mV at the output of RF oscillator and attenuated by ≈ 60 dB with attenuators and directional coupler, which results in ≈ 70 dBm of power applied to MN. The reflected signal is amplified by ≈ 70 dB before reaching the input of the lock-in. In correlation with results obtained for $\Delta|\Gamma|$ signals (Fig. 7a,b), the magnitude of SB signals is very significantly boosted by appropriate choice of MN.

In fact, the magnitude of SB for $C_{IN} = 30$ pF is scaled up by a factor > 15 compared to $C_{IN} = 0$ pF. Direct acquisition of SB signals also allows optimization of the operating carrier frequency by finding the maximum of

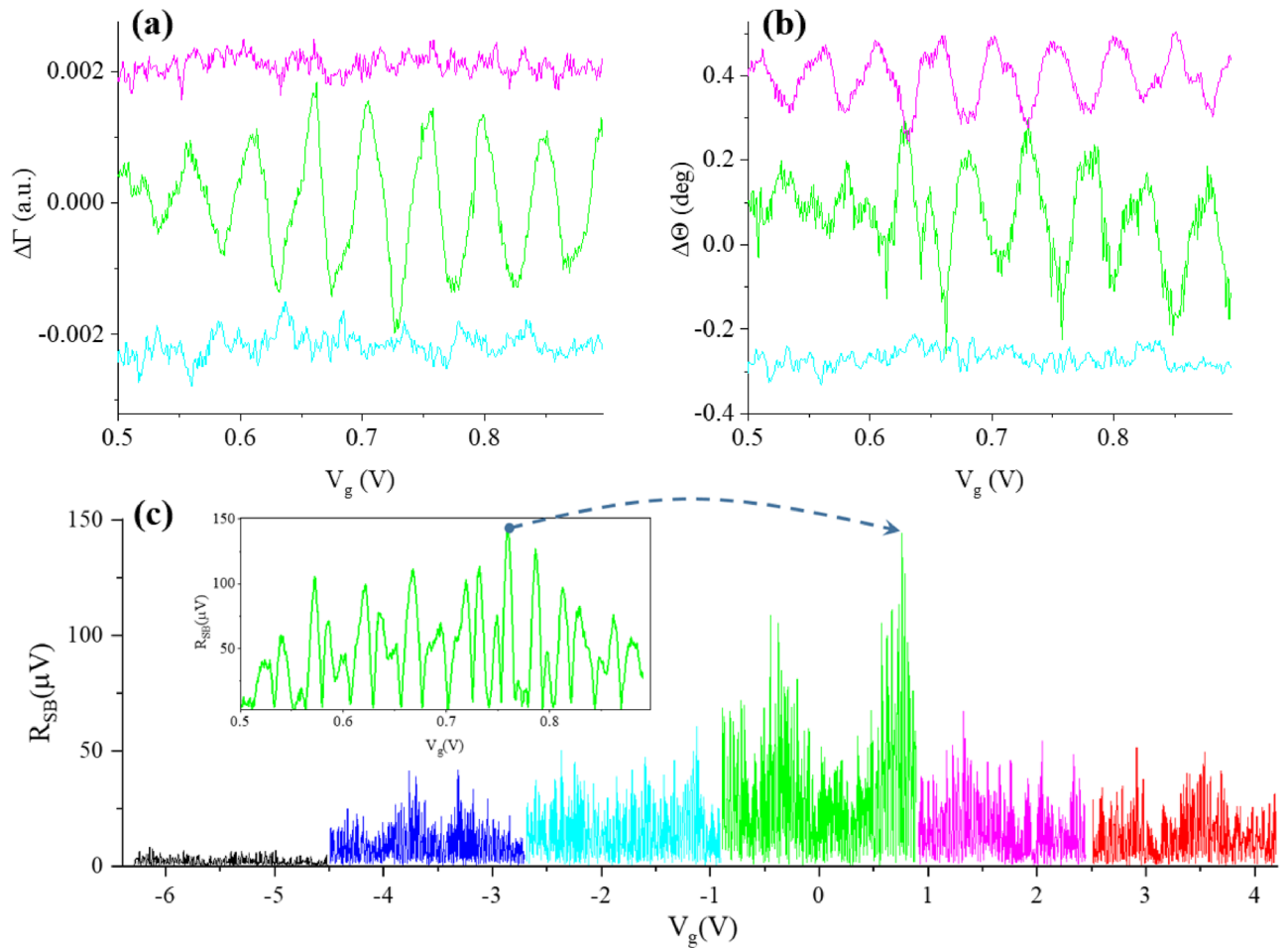


Figure 7. Coulomb blockade oscillations $Y(V_g)$ of the SEBA measured as magnitude **(a)** and phase **(b)** of reflection at the operating frequency f_{Op} using ECD for three values of the balancing capacitor C_{IN} : 15 pF (light blue), 30 pF (green), 45.8 pF (magenta). Constant values of magnitude and phase are subtracted from each curve to eliminate DC offset and curves are further vertically offset for clarity. Each trace is acquired with 40 ms time constant, no trace averaging is performed. No modulating signal is applied. **(c)** Comparison of SEBA oscillations $Y(V_g)$ detected as SB magnitudes for modulating signal $\approx 0.07e$ applied to the gate of SEBA obtained for six cases of C_{IN} : 0 pF (black); 6.8 pF (blue); 15 pF (light blue); 30 pF (Green); 45.6 pF (magenta); 60 pF (red). Curves are horizontally offset for clarity. $T=3.6K$. Inset: zoom into beating oscillation pattern for $C_{IN}=30$ pF. The arrow points to the working point for $C_{IN}=30$ pF, $V_g=0.759V$.

the magnitude of SB signals. Fig. 8 shows a frequency response of MN, $|\tilde{\Gamma}|(f_{carrier})$ (black dots) and both upper (red dots) and lower SB (blue dots) for low frequency modulation applied to the gate. As expected, the maxima in SB are in perfect correlation with the minimum in the magnitude of reflected carrier signal.

Once SEBA oscillations in SB are characterized and optimal operation frequency f_{Op} is found, for each value of C_{IN} the strongest peak in demodulated SB signal $R_{SB}(V_g)$ is identified at some $V_g = V_{g0}$ within $\pm 0.9V_g$ span (inset in Fig. 7c), and the bandwidth available with this setting of C_{IN} for SEBA sensing is characterized at this V_{g0} . For that purpose the frequency response of SEBA to the modulation frequency f_{Mod} is measured using setup Fig. 2a by acquiring SB signals as we sweep modulation frequency f_{Mod} in the range 1 kHz–20 MHz for each value of C_{IN} . It is important to note that the carrier frequency needs to be chosen appropriately for each setting of C_{IN} . Figure 9a–c shows frequency response of the SEBA in the upper and lower SB measured for three different settings of carrier frequency. If carrier frequency f_{RF} is chosen 2 MHz below (above) the optimal $f_{Op} = 402.608$ MHz, the resulting SB signals are greatly attenuated at all modulation frequencies except near $f_{RF} = f_{Op} + f_{Mod}$ for the lower SB, subplot Fig. 9c (or near $f_{Op} - f_{Mod}$ for the upper SB, subplot Fig. 9a), when the resulting tone lands in the pass-band near f_{Op} . When f_{Op} is chosen at the minimum of Γ (obtained using ECD protocol), the magnitude of both sidebands stays constant at ≈ -85 dBV level within ≈ 1 MHz until the -3 dB level is reached at $f_{Mod} \approx 1.2$ MHz Fig. 9b. Clearly, the choice of appropriate carrier frequency, $f_{RF} = f_{Op}$, yields the strongest response within the entire pass-band.

These measurements combined together enable direct comparison of the magnitude of SB signals generated at different C_{IN} settings over the sensing BW of interest. Figure 9d provides a composite 2D picture for tuning of the MN with balancing capacitor C_{IN} . Here, the color-coded strength of the relative SB magnitude referred to applied RF signal (in dB) in response to modulating signal is plotted vs modulating frequency f_{Mod} (X axis)

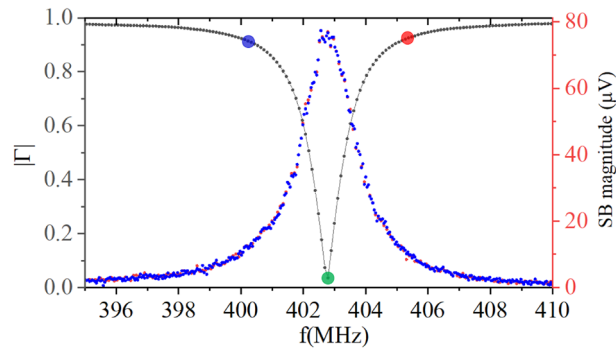


Figure 8. Error-corrected magnitude of reflection $|\Gamma|$ (in black) and magnitudes of demodulated sidebands (lower SB - blue dots, upper SB - red dots) vs carrier frequency for MN connected to SEBA with $L = 240$ nH and $C_{IN} = 30$ pF. The signal is measured at the input of the UHFLIA in Fig. 2a. Sinusoidal signal \tilde{V}_g at $f_{Mod} = 8$ kHz with RMS value of 3.5 mV is applied to the gate of SEBA along with a constant $V_{g0} = 0.879$ V, positioning the response of the SEBA at the peak in SB signal in Fig. 7c. The three selected operation frequencies are shown by blue (400.6 MHz), green (402.6 MHz) and red (404.6 MHz) dots. $T = 3.6$ K.

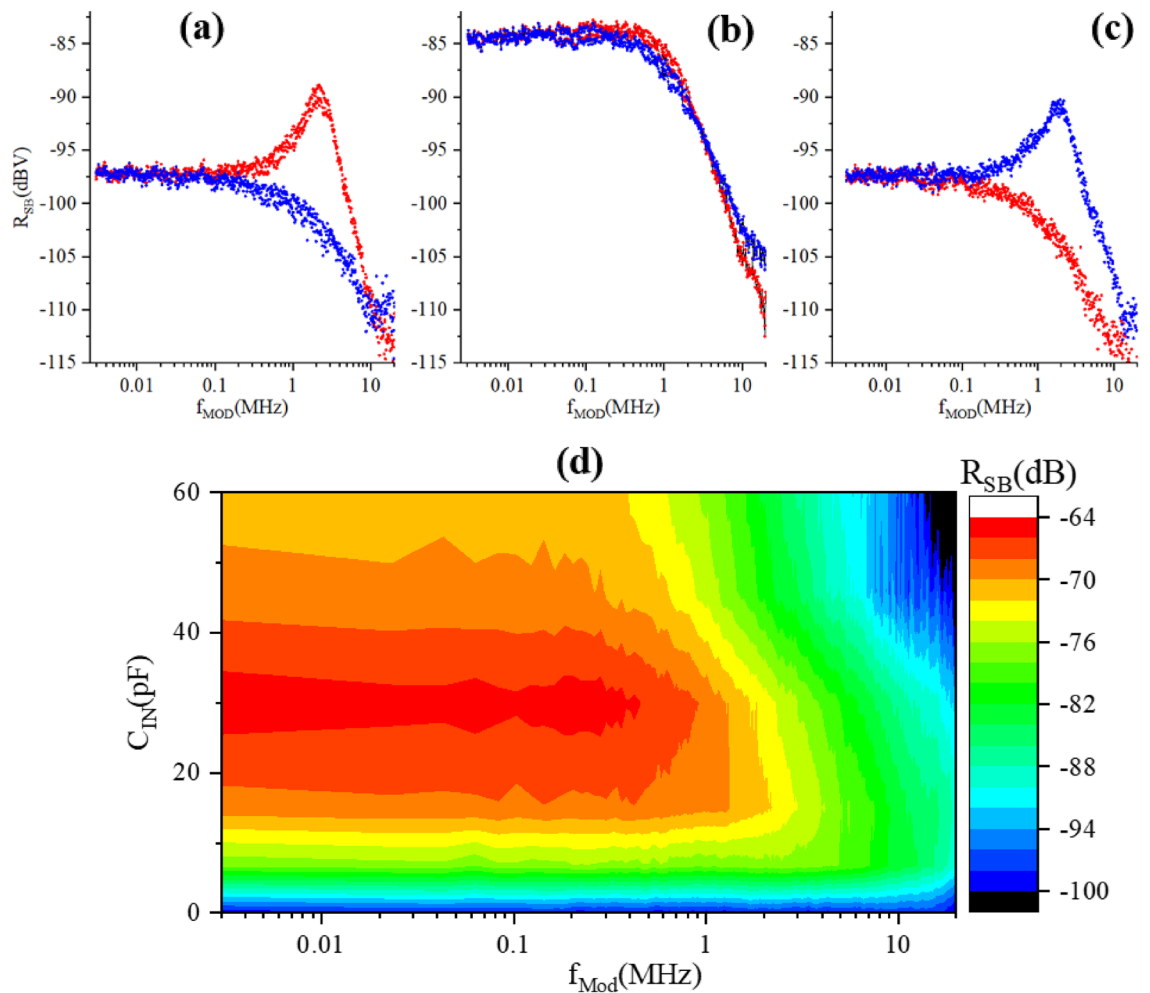


Figure 9. RMS value of upper (red) and lower (blue) SB vs modulation frequency f_{Mod} . $\tilde{V}_g = 3.5$ mV RMS measured at the input of UHFLIA using setup Fig. 2a; for well-matched case $C_{IN} = 30$ pF with resonant frequency of 402.608 MHz. Subplots a-c correspond to different carrier frequencies 400.6 MHz (a); 402.6 MHz (b); 404.6 MHz (c), marked by dots in Fig. 8. (d) Color map showing experimentally obtained relative SB magnitude (in dB) vs frequency of modulating sinusoidal signal \tilde{V}_g applied to the gate of SEBA for chosen input C_{IN} . Carrier frequency for each C_{IN} is adjusted to obtain maximal SB magnitude at low modulation frequency $f_{Mod} < 10$ kHz (see Fig. S8b in Supplementary materials for the exact values of carrier frequency). Color represents normalized magnitude of SB. For normalization the carrier signal level out of resonance 395 MHz and 410 MHz in Fig. 8 for $C_{IN} = 30$ pF is taken as 0 dB. Temperature of experiment is 3.6 K.

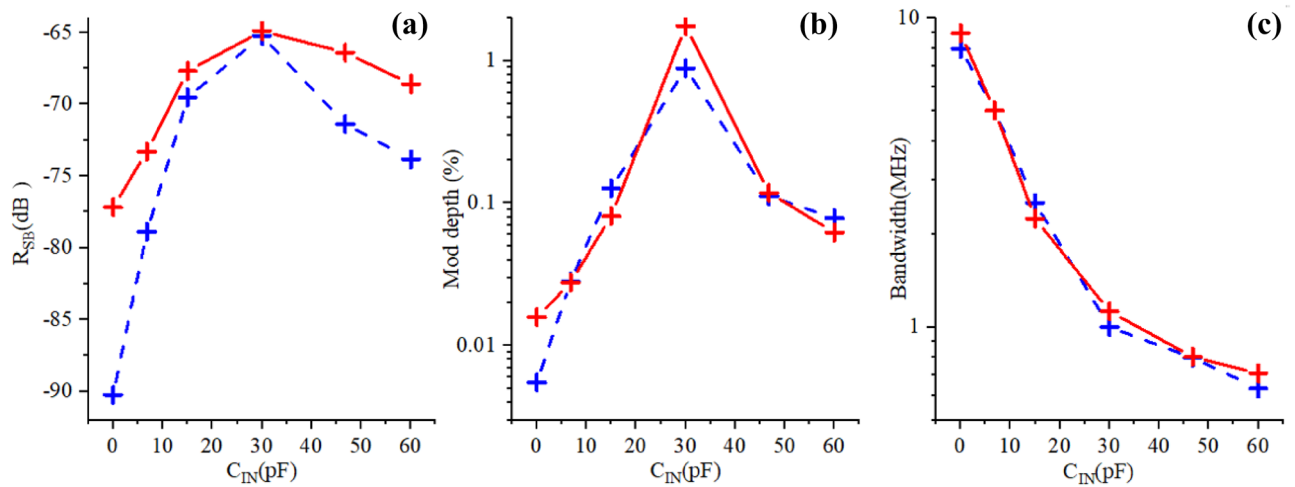


Figure 10. Three important parameters plotted vs balancing capacitor C_{IN} . Red crosses with solid lines—simulation, blue crosses with dashed lines—experiment. Left: SB magnitude normalized to $C_{IN} = 30$ pF case. Middle: Modulation depth, in percent; $\tilde{V}_g = 3.5$ mV at $f_{Mod} = 8$ kHz. RF carrier magnitude before attenuation is 65 mV peak for all C_{IN} , except for $C_{IN} = 0$ where it is 300 mV peak to account for low SNR. Right: Bandwidth (on -3 dB level) f_{Mod} available for SEBA sensing. Note that here the experimental data are not subjected to calibration/error correction.

and balancing capacitor C_{IN} (Y axis). One can see that for $C_{IN} = 0$, when the matching network is out of tune, the relative magnitude of the generated side band signal is the smallest: the signal (blue) is ≈ -97 dB, i.e. about 24 dB weaker compared to well-matched case (red), where it reaches ≈ -64 dB. As the value of C_{IN} increases from 0 to $C_{IN} = 30$ pF ($\approx C_{match}$), closest to the matching conditions, the strength of the SEBA response in the pass-band also increases, but at the same time its bandwidth shrinks. Further increase of C_{IN} beyond C_{match} monotonically reduces the magnitude of the gate response and it continues to reduce the available bandwidth. Therefore, by using $C_{IN} = C_{match}$ one achieves the best trade-off between sensitivity and bandwidth. These experimental results are in good qualitative correlation with the simulations (see supplementary information, plot S9). To perform simulations of the sideband signal the response of SEBA admittance to the input \tilde{V}_g is first simulated and the working point is defined (see part S5 in the Supplementary information for details). Next, the admittance equivalent of SEBA is connected to the MN simulated using optimized inductor model and its response to the modulating signal, $\tilde{V}_g = 3.5$ mV RMS, is calculated for f_{Mod} in the frequency range, 1 kHz–20 MHz (see part S6 in the Supplementary information for details).

Note that error-corrected data in this work are only available for the carrier frequency signal because CEC protocol is only performed for demodulated f_{RF} which is schematically represented a $[e]^{-1}$ box in Fig. 2a. This precludes a direct numerical comparison of experimentally acquired side-band signals with simulations, except perhaps the case where MN is close to matching and error-correction is minimal. Nonetheless simulations provide a good way to look at the performance of SEBA connected to MN in terms of magnitude and bandwidth of generated sidebands. In our future work we plan to embed CEC protocol into SB demodulation path using Zurich instruments software²⁷.

Therefore in this work direct quantitative comparison between experiment and calculation cannot be performed for SB and only qualitative analysis is possible. Indeed, the simulations assume an ideal network analyzer, while in experiment the performance of MN, particularly for C_{IN} close to zero suffers from various non-idealities, e.g. destructive interference in the standing waves in the cables. Therefore, simulations underestimate the loss of signal away from the match point. This is clearly illustrated in Fig. 10a where simulations predict significantly smaller signal degradation for C_{IN} approaching zero.

The experimentally obtained and simulated modulation depth, defined as a ratio of $SB/Carrier$ magnitudes, and expressed in percents, is plotted vs C_{IN} in Fig. 10b. Experiment and simulations are in good correlation, except for small values of C_{IN} where simulated modulation depth overestimates the performance due to assumed ideal reflectometer. In either case the modulation depth is very low for $C_{IN} = 0$ ($\approx 10^{-2}\%$), it reaches maximum of $\approx 1\%$ for $C_{IN} = 30$ pF, for closest to match conditions and then goes down again but at a less steep pace for balancing capacitor values that exceed the optimal. Very small modulation depth implies very inefficient energy transfer to and from DUT, and ultimately reduces the dynamic range for measurements of $|\Gamma|$ due to a large constant (i.e. V_g independent) value after demodulation. Finally, Fig. 10c shows very good correlation between experiment and simulations for the BW accessible for SEBA sensing.

The results presented in Fig. 10 clearly demonstrate that the sensitivity drops abruptly for $C_{IN} \ll C_{match}$ but enables a broader flat portion of available bandwidth while for $C_{IN} > C_{match}$ the monotonic drop in sensitivity is accompanied by a significant loss of bandwidth. Here C_{match} is the optimal value of C_{IN} which provides closest to match settings of MN.

Conclusions

We propose and demonstrate a simple two-step method for optimizing Π MNs for low temperature reflectometry of large ($\gg 1\text{M}\Omega$) DUT impedances. By performing a measurement of the partial MN utilizing an inductor L with unknown parasitics and capacitance C_{pad} in parallel to a DUT, a balancing capacitor C_{IN} can be found as long as the partially assembled MN with attached DUT represents a load overcoupled to the feed line, the condition fulfilled for nearly all studied inductors of the 0805LS series¹⁵. This method requires a low temperature calibration of the reflectometer in order to remove effects of non-idealities in the reflectometer, and leads to more numerically meaningful measurements. Performing a low temperature calibration is a time-consuming process requiring multiple thermal cycles of a cryostat. Because of this, there is inevitable error present in the error correction model that ends up in the final error corrected data. However, these errors are small enough that the error corrected data can still be used to produce meaningful results.

Experiment also shows that to achieve quantitative accuracy the simulations performed to model matching networks must take into consideration parasitic components of the inductors used in MN^{12,13}, and neglecting these parasitics leads to significant errors in the evaluation of sensitivity and bandwidth. We compare the simulations results of two models (see part S7 in supplementary materials for more details). Model A used in this work and^{12,13} takes into account low-temperature values of parasitic components while model B^{1,3} utilizes an ideal inductor and a leakage resistance R_d in parallel to C_{pad} introduced to account for experimentally observed losses revealed by a presence of a dip in the magnitude of reflection coefficient Γ . Figure S11 in Supplementary materials confirms the validity of approach used in this work.

Our measurements demonstrate that achieving a good match can have a very significant impact on the ability to measure weak signals. This is clearly demonstrated by performing a detailed comparison of the SB magnitudes for different settings of Π MN tuned by a balancing capacitor C_{IN} : the SB signal strength is greatly enhanced when the close to match conditions are achieved. Experiments have shown that the SB signal enhancement exceeds 20 dB compared to “as is” MN with $C_{IN} = 0$. The underlying physical reason for such improvement is that by achieving close to match conditions we achieve the most efficient energy transfer when the load to the feedline is closest to Z_0 . As a result, the negative impacts of various non-idealities in this situation are canceled to a large degree in contrast with grossly mismatched conditions where these non-idealities such as destructive interference only exacerbate the existing mismatch.

Both experiment and simulations show that the presence of balancing capacitor C_{IN} shapes the bandwidth available for DUT operation and BW is monotonically reduced with the increase in C_{IN} . By contrast, the magnitude of detected SB increases rapidly for $C_{IN} < C_{match}$, and slowly decreases for $C_{IN} > C_{match}$.

Data availability

The data that support the findings of this study are available from the corresponding author upon reasonable request.

Received: 15 June 2021; Accepted: 2 February 2022

Published online: 23 February 2022

References

- Gonzalez-Zalba, M. F., Barraud, S., Ferguson, A. J. & Betz, A. C. Probing the limits of gate-based charge sensing. *Nat. Commun.* **6**, 8 (2015).
- Crippa, A. *et al.* Level spectrum and charge relaxation in a silicon double quantum dot probed by dual-gate reflectometry. *Nano Lett.* **17**, 1001–1006 (2017).
- Ibberson, D. J. *et al.* Low-temperature tunable radio-frequency resonator for sensitive dispersive readout of nanoelectronic devices. *Appl. Phys. Lett.* **114**, 123501 (2019).
- Ahmed, I. *et al.* Radio-frequency capacitive gate-based sensing. *Phys. Rev. Appl.* **10**, 014018 (2018).
- Ahmed, I. *et al.* Primary thermometry of a single reservoir using cyclic electron tunneling to a quantum dot. *Commun. Phys.* **1**, 66 (2018).
- Colless, J. I. *et al.* Dispersive readout of a few-electron double quantum dot with fast rf gate sensors. *Phys. Rev. Lett.* **110**, 046805. <https://doi.org/10.1103/PhysRevLett.110.046805> (2013).
- Zimmerman, N. M. & Keller, M. W. Dynamic input capacitance of single-electron transistors and the effect on charge-sensitive electrometers. *J. Appl. Phys.* **87**, 8570–4 (2000).
- Mizuta, R., Otxoa, R. M., Betz, A. C. & Gonzalez-Zalba, M. F. Quantum and tunneling capacitance in charge and spin qubits. *Phys. Rev. B* **95**, 045414 (2017).
- Persson, F., Wilson, C. M., Sandberg, M., Johansson, G. & Delsing, P. Excess dissipation in a single-electron box: The sisyphus resistance. *Nano Lett.* **10**, 953–957 (2010).
- Ciccarelli, C. & Ferguson, A. J. Impedance of the single-electron transistor at radio-frequencies. *New J. Phys.* **13**, 093015 (2011).
- Frake, J. C. *et al.* Radio-frequency capacitance spectroscopy of metallic nanoparticles. *Sci. Rep.* **5**, 10858 (2015).
- Filmer, M. J., Zirkle, T. A., Chisum, J., Orlov, A. O. & Snider, G. L. Using single-electron box arrays for voltage sensing applications. *Appl. Phys. Lett.* **116**, 213103 (2020).
- Zirkle, T. A. *et al.* Radio frequency reflectometry of single-electron box arrays for nanoscale voltage sensing applications. *Appl. Sci.* **10**, 8797. <https://doi.org/10.3390/app10248797> (2020).
- Schoelkopf, R. J., Wahlgren, P., Kozhevnikov, A. A., Delsing, P. & Prober, D. E. The radio-frequency single-electron transistor (rf-set): A fast and ultrasensitive electrometer. *Science* **280**, 1238–42 (1998).
- Coilcraft Industries, inc. Spice model -0805cs https://www.coilcraft.com/getmedia/c86a99da-e310-4932-bb03-09af08346f8a/spice_0805cs.pdf (2012).
- Roschier, L. *et al.* Noise performance of the radio-frequency single-electron transistor. *J. Appl. Phys.* **95**, 1274–86 (2004).
- Pozar, D. M. *Microwave Engineering* (Fourth edition. Hoboken, NJ : Wiley, [2012] ©2012, 2012). Includes bibliographical references and index.
- Ares, N. *et al.* Sensitive radio-frequency measurements of a quantum dot by tuning to perfect impedance matching. *Phys. Rev. Appl.* **5**, 034011 (2016).

19. Mizokuchi, R., Bugu, S., Hirayama, M., Yoneda, J. & Kodera, T. Radio-frequency single electron transistors in physically defined silicon quantum dots with a sensitive phase response. *Sci. Rep.* **11**, 5863 (2021).
20. Chisum, J. D. & Popovic, Z. Performance limitations and measurement analysis of a near-field microwave microscope for non-destructive and subsurface detection. *IEEE Trans. Microwave Theory Tech.* **60**, 2605–2615. <https://doi.org/10.1109/TMTT.2012.2201739> (2012).
21. Ranzani, L., Spietz, L., Popovic, Z. & Aumentado, J. Two-port microwave calibration at millikelvin temperatures. *Rev. Sci. Instrum.* **84**, 034704 (2013).
22. Lafarge, P. *et al.* Direct observation of macroscopic charge quantization. *Z. Phys. B* **85**, 327–332 (1991).
23. Brenning, H. T. A. *et al.* A single electron transistor on an atomic force microscope probe. *Nano Lett.* **6**, 937–941. <https://doi.org/10.1021/nl052526t> (2006).
24. Suter, K. *et al.* Integration of a fabrication process for an aluminum single-electron transistor and a scanning force probe for tuning-fork-based probe microscopy. *J. Microelectromech. Syst.* **19**, 1088–1097. <https://doi.org/10.1109/JMEMS.2010.2067198> (2010).
25. Gustavsson, S., Gunnarsson, D. & Delsing, P. Cryogenic amplifier for intermediate source impedance with gigahertz bandwidth. *Appl. Phys. Lett.* **88**, 153505. <https://doi.org/10.1063/1.2194820> (2006).
26. Dolan, G. J. Offset masks for lift-off photoprocessing. *Appl. Phys. Lett.* **31**, 337–339. <https://doi.org/10.1063/1.89690> (1977).
27. Zurich Instruments, U. U. m. Uhf-mod am/fm modulation option https://www.zhinst.com/sites/default/files/documents/2020-08/ziUHF_UserManual_20.07.0.pdf (2021).

Acknowledgements

This work was supported by the National Science Foundation Grants ECCS-1509087 and DMR-1904610. Any opinions, findings, and conclusions or recommendations expressed in this material are those of the author(s) and do not necessarily reflect the views of the National Science Foundation. Authors are grateful to Dr. Eva Dupont-Ferrier for multiple useful discussions. All figures were drawn by the authors.

Author contributions

M.F., A.O. and G.S. conceived the experiments, T.Z. designed and fabricated the devices (SEBA), M.S. and X.J. designed and fabricated the RF boards, M.H. and A.O. conducted the experiments, M.F. conceived and implemented BW and SB simulation protocols and the wrote the scripts for error correction, J.C. conceived the MN optimization protocol and supervised high frequency experiments, M.H., M.F., J.C. and A.O. analysed the results. M.F., M.H. and A.O. wrote the manuscript. All authors reviewed and revised the manuscript.

Competing interests

The authors declare no competing interests.

Additional information

Supplementary Information The online version contains supplementary material available at <https://doi.org/10.1038/s41598-022-06727-1>.

Correspondence and requests for materials should be addressed to M.J.F.

Reprints and permissions information is available at www.nature.com/reprints.

Publisher's note Springer Nature remains neutral with regard to jurisdictional claims in published maps and institutional affiliations.



Open Access This article is licensed under a Creative Commons Attribution 4.0 International License, which permits use, sharing, adaptation, distribution and reproduction in any medium or format, as long as you give appropriate credit to the original author(s) and the source, provide a link to the Creative Commons licence, and indicate if changes were made. The images or other third party material in this article are included in the article's Creative Commons licence, unless indicated otherwise in a credit line to the material. If material is not included in the article's Creative Commons licence and your intended use is not permitted by statutory regulation or exceeds the permitted use, you will need to obtain permission directly from the copyright holder. To view a copy of this licence, visit <http://creativecommons.org/licenses/by/4.0/>.

This is a U.S. Government work and not under copyright protection in the US; foreign copyright protection may apply 2022